Research Square

Preprints are preliminary reports that have not undergone peer review.
They should not be considered conclusive, used to inform clinical practice,
or referenced by the media as validated information.

Defect-tolerant anti-fatigue titanium alloy via multi-scale heterogeneous interface engineering

Jian-Chao Pang

jcpang@imr.ac.cn

Institute of Metal Research, Chinese Academy of Sciences https://orcid.org/0000-0002-8409-8281

Xiao-Yuan Teng

Institute of Metal Research, Chinese Academy of Sciences

Cheng-Lu Zou

Institute of Metal Research, Chinese Academy of Sciences

Zhe-Feng Zhang

Institute of Metals Research, Chinese Academy of Sciences https://orcid.org/0000-0001-5674-2415

Article

Keywords:

Posted Date: June 1st, 2026

DOI: https://doi.org/10.21203/rs.3.rs-9853700/v1

License: This work is licensed under a Creative Commons Attribution 4.0 International License.
Read Full License

Additional Declarations: There is **NO** Competing Interest.

Abstract

Additive manufacturing (AM) offers unparalleled design freedom and processing efficiency for titanium alloys, yet widespread adoption is hindered by poor fatigue performance originating from inevitable microvoids. In this study, we break this paradigm by introducing a post-processing strategy based on interface engineering. By exploiting the synergy between AM-induced metastable microstructures and rapid thermal processing (RTP), we construct a multi-scale heterogeneous interface network (MHIN) in a Ti-6.5Al-3.5Mo-1.5Zr-0.3Si alloy. This MHIN architecture delivers exceptional defect tolerance through a "compartmentalized plasticity" mechanism, achieving a high-cycle fatigue (HCF) strength of 955 MPa at 25 ℃ and, remarkably, 704 MPa at 500 ℃, the highest values ever reported for any titanium alloy at these temperatures. This new finding demonstrates that interface engineering can decouple fatigue resistance from void density, providing a generalizable pathway to qualify AM components for safety-critical applications across a wide temperature range.

Main

Despite the acknowledged mechanical properties of additively manufactured (AM) titanium alloy, its widespread adoption is critically hampered by a persistent shortcoming: the inferior fatigue resistance of AM alloy compared to its forged counterparts [1]. It is generally accepted that inevitable AM-induced defects undermine the otherwise dense microstructure, drastically reducing fatigue properties from its theoretical potential. This long-standing insight has guided fatigue resistant design for AM alloys toward attaining fully dense, defect-free microstructures, where hot isostatic pressing (HIP) has consequently been regarded as an indispensable processing step in the previous investigations [2-5]. Yet the evidence indicates that, despite its efficacy in closing microvoids [6, 7], HIP still fails to fully mitigate the adverse influence of microvoids on fatigue properties [4, 8], a shortcoming that is particularly evident during operation at elevated temperatures [9]. In fact, HIP improves density by compressing rather than removing or dissolving [10, 11]. Consequently, the treated AM alloy may present a deceptively near-void-free microstructure while still containing trapped gas. Despite their reduced volume, these microvoids can be re-opened due to the high thermal expansion coefficient of the trapped gas, which generated significant internal pressure during post-treatments or service at elevated temperatures, continuing to drive fatigue failure.

A complementary strategy is imperative: rather than focusing solely on complete defect elimination, the AM microstructure itself should be strengthened to tolerate, or even negate, the damaging influence of residual microvoids. This concept of "defect tolerance through matrix optimization" originates from concerns over microvoids that persist after HIP, particularly for alloys designed for high temperature service. The exceptional strengthening effect of interfaces has been long acknowledged in the materials science community [12, 13]. Their strengthening benefits, achieved via suppression of dislocation motion and resistance to micro-deformation at ambient temperature [14], have been extensively documented across various interface types, including grain boundaries (GBs) [15-18], phase boundaries (PBs) [19-21], metastable interfaces [22-24], and twin boundaries (TBs) [25-27]. The intrinsic link

between tensile and high-cycle fatigue (HCF) behavior has also been well established [28]. Notably, interface engineering still dominates as a reinforcement strategy at 500 °C [29], with the strengthening effect far outweighing any slip-induced degradation.

Extending interface engineering, we propose a multi-scale heterogeneous interface network (MHIN) microstructural design concept. It is engineered to be macroscopically uniform, ensuring the elimination of single weak regions that could dominate fatigue failure, while its microscopically heterogeneous, multi-scale interfaces are interconnected into a network that progressively blocks dislocations [30] and tolerate AM-induced microvoids under cyclic stress. The overarching function of this design is to enable "compartmentalized plasticity", wherein fatigue damage is confined to isolated sacrificial zones, thereby decoupling plastic strain accommodation from damage accumulation. During solution treatment above the β-transus, titanium alloy transforms from α to β via diffusional nucleation and growth, creating a transient microstructure rich in α/β and β grain boundaries [31, 32]. By applying a sufficiently high cooling rate, this high-density interface state is partially inherited, leading to the formation of a fine-scale, hierarchical microstructure consisting of either α/β lamellar colonies (Widmanstätten) or α'/α" martensitic laths, depending on the alloy composition and cooling path. Here, we attempt to capture this transient high-density interface state within the narrow interval of phase transformation and stabilize it down to room temperature for achieving the MHIN microstructure. Rapid thermal processing (RTP), which precisely controls ultra-fast heating and cooling cycles, offers a practical means to realize this high undercooling condition. We therefore employ this method to obtain the MHIN microstructure, where ultra-fast heating enables the formation of high-density interfaces [33, 34] that are preserved at ambient temperature by an ultra-fast cooling cycle.

In summary, the RTP route successfully constructs a MHIN microstructure in the Ti-6.5Al-3.5Mo-1.5Zr-0.3Si alloy, characterized by high-density PB, GB, and nanotwins. The resulting microstructure exhibits superior fatigue resistance at both ambient temperature and 500 °C. Remarkably, this exceptional fatigue resistance is achieved even in the presence of residual microvoids unambiguously demonstrating genuine defect tolerance. Our new findings mitigate long-standing concerns about fatigue degradation caused by AM-induced microvoids and establish the MHIN design as a generalizable pathway toward reliable AM titanium alloys for safety-critical applications.

MHIN microstructure

This study introduces a paradigm shift in addressing fatigue defect tolerance design in AM titanium alloys: moving from complete defect elimination to defect tolerance via matrix optimization. The advantage of this concept holds across a broad temperature spectrum, from ambient 25 °C to elevated 500 °C, where thermal softening reduces stress concentration sensitivity around microvoids, mitigating their detrimental impact. The key lies in the MHIN microstructure, which realizes compartmentalized plasticity under cyclic stress by confining dislocation movement to limited areas, thereby avoiding damage accumulation while tolerating microvoids. This design is implemented through a tailored RTP

route: AM near-net shaping first establishes fine prior β grains, followed by HIP for densification and anisotropy reduction, and finally a precisely controlled RTP cycle triggers the β→α'/α" transformations, capturing the transient high-density interface state. The approach is fundamentally guided by the principle of suppressing dislocation motion and accumulation, a cornerstone for anti-fatigue titanium alloys [35-39], with the RTP step deliberately tailoring the MHIN to function as multi-scale hierarchical barriers. The schematic diagrams of the MHIN microstructure are shown in Fig. 1a.

Microstructural analysis (Figs. 1b-f) reveals the resulting MHIN characteristics. **(i) Refined prior-β grains.** The AM-derived prior-β grains remain fine and uniform, free from the GB migration often seen in conventionally processed alloy (Fig. 1b). This refined grain structure provides the first level of strengthening, effectively impeding dislocation motion. **(□) Mutually constrained α' colonies.** Within these grains, RTP promotes the formation of α' colonies and lamellae that nucleate at prior β GBs and grow inward. Notably, colonies of different orientations mutually constrain each other's growth, preventing any single variant from dominating (Fig. 1c), which creates a geometrically necessary interface network that impedes dislocation transmission across the lamellar structure. **(□) High-density α' interfaces.** Extreme undercooling drives a high nucleation density of α' martensite with limited growth under rapid cooling, which yields a dispersion of ultrafine, acicular α' between the lamellae, substantially increasing the interfacial density (Fig. 1d). The resulting high density of α' interface acts as a dense network of dislocation obstacles that elevates the stress required for plastic deformation, delaying fatigue crack initiation. **(□) Orthorhombic α" martensite.** Mo stabilizes β and favors a diffusion-influenced pathway over purely shear-based β→α' reaction, producing fine α" martensite (Fig. 1e). These α" interfaces introduce additional lattice mismatches, further impeding dislocation glide and enhancing damage tolerance. **(□) Coherent nanotwins.** Generated during the rapid β→α' phase transformation (Fig. 1f), these nanotwins feature low interfacial energy and high thermal stability, and efficiently block dislocation movement, suppressing persistent slip bands. Quantitative analysis of the two-phase morphology and microvoids is presented in Fig. S4.

Collectively, these five features assemble an MHIN microstructure that presents dislocation motion with an escalating cascade of interface barriers. A moving dislocation emerging around microvoids must sequentially overcome nano-scale precipitates/twins, sub-micron α/β interfaces, micro-scale α colony boundaries, and finally the macroscopic prior β GBs. The fatigue resistant design concept of the alloy is rooted in an MHIN microstructure that barriers dislocation motion and compartmentalizes local plastic deformation. Micro-defects, rather than triggering widespread failure, generate only confined, low-magnitude stress concentrations that are readily absorbed by the surrounding hierarchical interfaces, from nano-precipitates to prior β GBs.

Tensile and fatigue properties

The tensile properties reveal a classic strength–ductility trade-off governed by temperature (Fig. 2a). Specifically, the alloy achieves tensile strengths of 1557 MPa at ambient temperature and 1037 MPa at

500 °C. Despite this exceptional strength, the MHIN microstructure inevitably leads to a strength-ductility compromise. At ambient temperature, the dense interface network effectively blocks dislocation motion, resulting in a sharp loss of ductility, as evidenced by cleavage fracture predominantly along prior β GBs (Supplementary Material, Section 3). In contrast, when tested at 500 °C, thermal activation promotes atomic diffusion and enhances dislocation mobility. This transition toward improved ductility is reflected in the fractured morphology, where dimpled features replace the cleavage pattern, indicating that dislocations are now capable of moving and accumulating, thereby imparting significantly greater plasticity than observed at ambient temperature.

The MHIN microstructure delivers exceptional fatigue performance, with fatigue strengths of 955 MPa at ambient temperature and 704 MPa at 500 °C (Fig. 2b), outperforming both its forged counterparts (Fig. 2c) and other titanium alloys designed for 500 °C service (Fig. 2d). This superior fatigue resistance originates from the MHIN microstructure. At ambient temperature, the refined prior β grains and dense α'/α" interfaces act as hierarchical barriers, impeding dislocation motion via fine grain strengthening and interface-mediated obstruction. At 500 °C, the thermally stable coherent twin boundaries and diffusion-influenced α" martensite maintain interfacial integrity, while the enhanced dislocation mobility promotes uniform deformation and delays crack initiation. As a result, the MHIN microstructure outperforms conventional forged counterparts and ranks among the top tier of high-strength titanium alloys when benchmarked against established tensile-fatigue strength relationships (Fig. 3a). Notably, the measured fatigue properties at 500 °C surpasses previously reported values for various titanium alloys (Fig. 3b), directly validating the efficacy of the MHIN design concept across a wide temperature range.

To understand the factors limiting fatigue life, we identified crack-initiation sites in detail (Supplementary Material, Section 4). Statistical analysis indicates that nearly all fatigue cracks initiated at AM-induced microvoids (Table S1), yet the absence of microstructural crack initiation sites suggests that the MHIN microstructure itself possesses superior fatigue resistance. This deviation from the crack initiation behavior of forged counterparts [40] underscores an intrinsic limitation in the fatigue performance of AM alloys. Their fatigue strength is ultimately governed by the presence of microvoids. Critically, these microvoids are extremely small (4~34 μm), rendering them less potent stress raisers, which can be effectively contained by the surrounding strong microstructure. This finding highlights the remarkable damage tolerance conferred by the MHIN architecture: even with these residual microvoids, the AM titanium alloy achieves outstanding fatigue performance at both ambient and elevated temperatures. The strengthening mechanism operates primarily by prolonging crack initiation period, which typically dominates total fatigue life. Among the tested samples, a few exhibited abnormally low fatigue life. Further analysis traced these failures to surface microvoids that initiated cracks (Fig. S6). In these cases, the crack initiation period is effectively bypassed, leaving only a brief propagation stage and resulting in premature failure. This contrast in fracture behavior further confirms the contribution of the MHIN microstructure to microvoids tolerance.

Mechanistic understanding of MHIN enhanced fatigue resistance

To explain this remarkable performance, we propose a unifying mechanistic concept termed as "compartmentalized plasticity." This concept posits that the MHIN design spatially segregates two critical functions: the accommodation of cyclic plastic strain within specific microstructural compartments and the isolation of this deformation to prevent its propagation across the microstructure. If this concept is valid, such a design should decouple plastic strain accommodation from fatigue damage accumulation, two processes that are intrinsically linked in conventional alloys, thereby enabling high fatigue resistance even in the presence of defects. The following sections test this hypothesis by examining dislocation behavior and interface responses at both ambient and elevated temperatures, using the experimental observations presented in Figs. 4 and 5.

Microstructure adjacent to microvoids along the loading direction is examined to track dislocation motion (Fig. 4a). Dislocation arrangements and barrier obstacles induced by cyclic loading are analyzed using the two-beam diffraction invisibility criterion. Observations in Figs. 4b and 4c reveal that limited dislocations within the ultrafine α' martensite emit along the [0002] direction (blue line), a behavior consistent with reported tensile-mode dislocation activity in titanium alloys [41]. This emission is driven by the tensile component of asymmetric cyclic stress (R>0), which maintains a sustained unidirectional load on the alloy, inducing dislocations primarily through a single slip system. Critically, this slip is strictly confined within the α' martensite lamellae, indicating that dislocation glide is effectively constrained by PBs [42] (green dotted line, Fig. 4b). This confinement is one of the components in the fatigue resistance: by restricting dislocation activity to isolated lamellar units, the MHIN microstructure prevents the formation of long-range slip bands that might otherwise propagate across GBs and coalesce into fatigue cracks.

Furthermore, a few dislocation lines marked by red arrows in the other α' lamella (Fig. 4c) are identified as <c>-type dislocations (*b* = [0001]) based on the two-beam invisibility criterion. To further investigate interface strengthening and dislocation motion, the high-resolution transmission electron microscope (HRTEM) image in Fig. 4e provides a high-magnification view of the region outlined in Fig. 4c. These analyses reveal key interfacial characteristics: fast fourier transform (FFT) diffraction identified it as an interface between two α’ lamellae sharing the same lattice orientation, while STEM-EDS (Fig. 4f) detected a Mo-rich zone at this boundary. By stabilizing the β phase, Mo contributes to the formation of dispersed strengthening boundaries that act as effective barriers to dislocation motion [43]. The effectiveness of this interface as a barrier against dislocation motion is directly demonstrated in Figs. 4h and 4i. The corresponding Inverse fast fourier transform (IFFT) images and geometric phase analysis (GPA) reveal that dislocation transmission traces and micro-deformation are confined to the grain boundary, unable to cross the adjacent Mo-rich zone [44]. This observation implies a critical mechanism: Mo-enriched PBs serve as impenetrable walls for dislocations, forcing them to accumulate at the interface rather than to propagate across it.

Fig. 4d reveals nanotwins at the α' phase, with the HRTEM image showing the adjacent nanoscale twin structure. By effectively blocking dislocation glide within α' lamellae, these twin boundaries suppress the formation of persistent slip bands, a critical precursor to fatigue crack initiation [45, 46]. IFFT analysis in Fig. 4g further elucidates the role of twin boundaries in fatigue resistance, revealing distinctly different dislocation motions on either side of the boundary and confirming their effectiveness in impeding dislocation motion. This localized confinement of dislocation activity prevents the accumulation of plastic strain that would otherwise concentrate at microstructurally weak sites, delaying the transition from microstructurally short cracks to long, propagating fatigue cracks.

The above observations validate the compartmentalized plasticity at ambient temperature: dislocation activity is confined to the ultrafine α' lamellae serve as discrete deformation compartments that accommodate cyclic strain, while Mo-enriched phase boundaries and nanotwins act as impermeable barriers that confine dislocation activity and prevent damage propagation. Whether this mechanism remains active at 500 °C, where thermal activation would be expected to promote dislocation motion, is therefore examined.

Similarly, the subsurface region near the fatigue crack initiation site (Fig. 5a) is examined. Within the lamellae, slip occurs predominantly along the [0002] direction, marked by significantly more slip bands than observed at ambient temperature (Fig. 5b). The $g \cdot b = 0$ two-beam invisibility criterion establishes that this slip results from the glide of <a>-type dislocations along this direction (Figs. 5b and c). HRTEM imaging (Fig. 5d) and FFT analysis (inset) identify the α' lamellar boundaries as semi-coherent. Subsequently, STEM-EDS further reveals the presence of Mo-enriched zones at these boundaries (Fig. 5e). This enrichment pattern persists from ambient to elevated temperatures, implying minimal Mo diffusion under thermal stress and, consequently, stable interfacial strength that continues to impede dislocation motion [43]. IFFT analysis provides direct evidence that dislocation transmission is contained by these Mo-rich interfaces (Fig. 5f) [47]. The observed traces are strictly confined to the [0002] direction within the enriched zones, showing no cross-boundary propagation. This confinement establishes a fundamental strengthening mechanism: Mo-stabilized PBs act as thermally stable barriers that maintain the capability of dislocation blocking even under the combined effects of thermal activation and cyclic loading.

Conversely, dislocation activity is far more pronounced inside the α' lamellae than at general GBs. A focused IFFT analysis of an internal slip zone (Figs. 5g and h) reveals a high density of edge dislocations (inset, Fig. 5h), with a transmission density significantly surpassing that near PBs. GPA analysis confirms that this high concentration of retained dislocations induces substantial localized micro-deformation during slip (Fig. 5i). This phenomenon reveals a critical mechanistic insight: dislocations are free to move, multiply, accommodate plastic strain, and provide necessary ductility within the α' lamellae, yet their activity is effectively confined to these intra-lamellar regions. The high density of retained edge dislocations indicates that these coarsened α' lamellae serve as "soft" deformation zones that absorb cyclic plasticity, while the surrounding Mo-stabilized interfaces act as "hard" barriers that prevent this deformation from propagating across the microstructure.

Collectively, these observations establish a unifying principle for fatigue resistance in the MHIN design: superior performance is achieved through a "compartmentalized plasticity" strategy, where α' lamellae serve as sacrificial deformation zones that accommodate cyclic strain, while semi-coherent interfaces, chemically stable interfaces (Mo-enriched zones), and nanotwins act as impermeable barriers that isolate this deformation and prevent damage propagation.

The MHIN architecture achieves superior fatigue resistance in the Ti-6.5Al-3.5Mo-1.5Zr-0.3Si alloy at both ambient and elevated temperatures through a synergistic combination of microstructure design and deformation resistance mechanisms. On the one hand, this resistance arises from the precise capture that the MHIN architecture exerts over traditional anti-fatigue design concepts: (i) Defect mitigation by HIP: HIP minimizes the detrimental effect of AM-induced microvoids by reducing size and aspect ratio (Table S1). This transforms potentially harmful stress concentrators into benign, near spherical microvoids, effectively raising the threshold for fatigue crack initiation; (ii) Interlocked lamellar confinement: The MHIN alloy is achieved through an interlaced lamellar structure (Figs. 1c and d), which ensures a balance of strength and ductility. This interlaced lamellar structure restricts dislocation activity within individual lamellae while preventing its propagation across phase boundaries, with mutually reinforcing lamellae of different orientations achieving synergistic strengthening [48]; (iii) Interface strengthening and stress redistribution: The MHIN imparts high intrinsic strength to the matrix while simultaneously disturbing the local stress field around microvoids. The dense interface network disperses stress concentrations over a larger volume, enhancing defect tolerance and reducing the effective driving force for crack nucleation. On the other hand, the MHIN architecture enforces compartmentalized plasticity mechanism that confines cyclic micro-deformation to individual plastic units, as evidenced by: (i) Confined slip and damage isolation: Hierarchical dislocation confinement that restricts slip to within the α' lamellae. The coarsened α' lamella acts as an independent deformation unit, effectively isolating fatigue damage and preventing its accumulation across the microstructure; (ii) Hierarchical dislocation barriers: The MHIN, ranging from nanometers to micrometers, progressively impedes the long-distance glide and accumulation of dislocations around microvoids. This hierarchical confinement forces dislocations to encounter successive barriers at progressively finer scales, exhausting their mobility before they can coalesce into a critical fatigue damage zone, thereby effectively delaying crack initiation. (iii) Thermally stable interface barriers: The Mo-enriched zones at phase boundaries exhibit minimal diffusion under thermal stress, preserving their structural integrity and dislocation-blocking capability at 500 °C. Unlike conventional GBs that weaken at high temperatures, these chemically stabilized interfaces continue to impede dislocation motion, providing sustained fatigue resistance under thermal activation.

In this study, we demonstrate a synergistic effect that enhanced fatigue resistance from ambient to elevated temperatures in a commercial titanium alloy containing residual microvoids, achieved through the combined use of AM and RTP. The resulting MHIN, comprising phase boundaries, grain boundaries, and nanotwin boundaries, operates on a core mechanism of compartmentalized plasticity: progressively impeding dislocation motion while imparting high tolerance to AM-induced defects such as microvoids. By fundamentally altering the material's micro-mechanical response to cyclic stress, this design arrests

fatigue damage at its earliest stage, delivering performance that surpasses the existing Ti alloys available at 500 °C. This paradigm offers a viable solution to the long-standing limitation poor fatigue resistance in AM alloys, with direct applicability to the fabrication of commercial titanium alloy components for the aerospace hot sector.

Methods

Sample preparation and microstructural design

Gas-atomized Ti-6.5Al-3.5Mo-1.5Zr-0.3Si powder, with a particle size distribution of 15-60 μm and chemical composition 6.24 wt% Al, 3.42 wt% Mo, 1.61 wt% Zr, 0.25 wt% Si and balance Ti, was used as the feedstock. Cylindrical geometry (Φ7 × 50 mm) samples were built by laser powder bed fusion (LPBF) on a BLT-S310 machine, employing a laser power of 400 W and a scan speed of 1000 mm/s. Oxidation and contamination were prevented by employing an argon atmosphere during fabrication, where kept the oxygen content below 100 ppm. A 67° interlayer rotation scanning strategy was applied. The laser spot diameter was 90 μm, and the layer thickness was 60 μm, respectively. The LPBF specimens were subjected to a 2-hour stress relief annealing in vacuum. Hot isostatic pressing (HIP) was conducted using a QIH48URC system to mitigate the detrimental effect of intrinsic microvoids on the fatigue behavior. The HIP treatment was ultimately carried out at 930 °C and 150 MPa in an argon atmosphere for 3 hours, followed by furnace cooling.

Metallographic analysis revealed a β-transus temperature of approximately 1005 °C for the Ti-6.5Al-3.5Mo-1.5Zr-0.3Si alloy (Supplementary Material, Section 1). To ensure precise control of the heating history for RTP, an automated device utilizing resistance heating was therefore developed (Fig. S2). RTP employed a treatment of 1020 °C for 8 min, following the procedure outlined in Supplementary Material, Section 2. Subsequently, the RTP-treated samples were aged at 500 °C for 6 hours.

Mechanical tests

Specimens were machined along the LPBF build direction. Tensile specimens had a 3 mm diameter and 15 mm gauge length, while high-cycle fatigue (HCF) specimens had a 3 mm diameter and 5 mm gauge length. All samples were mirror-polished prior to testing, ensuring Ra < 0.2 μm, to reduce the impact of surface flaws. Tensile and HCF tests were conducted in accordance with ISO 6892-1:2019, ISO 6892-2: 2018, and ISO 1099: 2017. Tensile tests were conducted at a strain rate of 1×10^{-4} s^{-1} using an Instron 8801 with a furnace. A minimum of three specimens were tested per condition to ensure reliability. HCF testing was carried out using a TESTRONIC resonant testing system with an integrated furnace. All tests were run under stress amplitude control at a stress ratio of $R = 0.1$ and a frequency between 90-95 Hz, with the alternating load error kept below 0.15%. To ensure thermal equilibrium, specimens were stabilized at 500 °C for 30 min before the elevated-temperature test. Testing continued until fracture or a run-out of 10^7 cycles.

Microstructure examination

For microstructural examination, samples were first etched in an aqueous solution containing 2% HF and 1% HNO_3 for 15-20 s and then observed using an Olympus DP73 optical microscope. Further characterization of the β grain size was performed via electron backscatter diffraction (EBSD) on a Zeiss Sigma-500 field-emission scanning electron microscope equipped with a SYMMETRY-S2 detector, using step sizes ranging from 0.15 to 1 μm; the acquired data were processed with Aztec Crystal software. Transmission electron microscopy (TEM) was carried out on FEI Tecnai F20 and Thermo Fisher Spectra 200 AC-TEM/STEM instruments at an acceleration voltage of 200 kV.

Fracture surfaces were examined using a Zeiss Sigma 500 scanning electron microscope operated at 20 kV. To investigate the microstructural origin and damage mechanism of fatigue crack initiation, site-specific samples were extracted from regions near the crack initiation site using an FEI Scios dual beam system for subsequent detailed characterization.

Declarations

Data availability

Data will be made available on request.

CRediT authorship contribution statement

X.Y. Teng: Investigation, Conceptualization, Methodology, Data Curation, Formal analysis, Visualization, Writing – original draft. J.C. Pang: Resources, Project administration, Conceptualization, Formal analysis, Supervision, Funding acquisition, Writing – review & editing. C.L. Zou: Writing – review & editing. Z.F. Zhang: Supervision, Funding acquisition, Writing – review & editing.

Declaration of Competing Interest

The authors declare that they have no known competing financial interests or personal relationships that could have appeared to influence the work reported in this paper.

Acknowledgements

This work is supported by National Natural Science Foundation of China (NSFC) under Grant Nos. 52321001, 52130002, U24A2037 and the Strategic Priority Research Program of CAS (XDB1420001).

Supplementary materials

Supplementary material associated with this article can be found in the supplementary materials file.

References

1. A. Bandyopadhyay, K.D. Traxel, M. Lang, M. Juhasz, N. Eliaz, S. Bose, Alloy design via additive manufacturing: Advantages, challenges, applications and perspectives, Mater. Today 52 (2022) 207-224.
2. Y.Z. Huang, T.G. Fleming, S.J. Clark, S. Marussi, K. Fezzaa, J. Thiyagalingam, C.L.A. Leung, P.D. Lee, Keyhole fluctuation and pore formation mechanisms during laser powder bed fusion additive manufacturing, Nat. Commun. 13(1) (2022) 1170.
3. A.A. Martin, N.P. Calta, S.A. Khairallah, J. Wang, P.J. Depond, A.Y. Fong, V. Thampy, G.M. Guss, A.M. Kiss, K.H. Stone, C.J. Tassone, J.N. Weker, M.F. Toney, T. van Buuren, M.J. Matthews, Dynamics of pore formation during laser powder bed fusion additive manufacturing, Nat. Commun. 10 (2019) 1987.
4. H. Masuo, Y. Tanaka, S. Morokoshi, H. Yagura, T. Uchida, Y. Yamamoto, Y. Murakami, Influence of defects, surface roughness and HIP on the fatigue strength of Ti-6Al-4V manufactured by additive manufacturing, Int. J. Fatigue 117 (2018) 163-179.
5. X.Y. Teng, J.C. Pang, X.H. Peng, H. Zhang, S.X. Li, Z.F. Zhang, High-cycle fatigue properties of near-defect-free titanium alloy treated by additive manufacturing and hot-isostatic pressing at different temperatures, Int. J. Fatigue 203 (2026) 109311.
6. J. Benzing, N. Hrabe, T. Quinn, R. White, R. Rentz, M. Ahlfors, Hot isostatic pressing (HIP) to achieve isotropic microstructure and retain as-built strength in an additive manufacturing titanium alloy (Ti-6Al-4V), Mater. Lett. 257 (2019) 126690.
7. T. Mukherjee, J.W. Elmer, H. Wei, T.J. Lienert, W. Zhang, S. Kou, T. DebRoy, Control of grain structure, phases, and defects in additive manufacturing of high-performance metallic components, Prog. Mater Sci. 138 (2023) 101153.
8. W.Q. Chi, W.J. Wang, H.C. Zhou, R.G. Yan, Y. Mikami, Multiscale modelling of additively manufactured Ti-6Al-4V alloy: Fatigue performance evaluation from material to structural level, Int. J. Fatigue 201 (2025) 109181.
9. M. Teschke, J. Moritz, J. Tenkamp, A. Marquardt, C. Leyens, F. Walther, Defect-based characterization of the fatigue behavior of additively manufactured titanium aluminides, Int. J. Fatigue 163 (2022) 107047.
10. S. Shao, M.J. Mahtabi, N. Shamsaei, S.M. Thompson, Solubility of argon in laser additive manufactured α-titanium under hot isostatic pressing condition, Comput. Mater. Sci. 131 (2017) 209-219.
11. W. Tillmann, C. Schaak, J. Nellesen, M. Schaper, M.E. Aydinöz, K.P. Hoyer, Hot isostatic pressing of IN718 components manufactured by selective laser melting, Addit. Manuf. 13 (2017) 93-102.
12. C.L. Zhang, X.Y. Bao, M.Y. Hao, W. Chen, D.D. Zhang, D. Wang, J.Y. Zhang, G. Liu, J. Sun, Hierarchical nano-martensite-engineered a low-cost ultra-strong and ductile titanium alloy, Nat. Commun. 13(1) (2022) 5966.
13. W.T. Chen, K.H. Wang, G. Liu, Enhancement of high-temperature performance in titanium alloys through rapid heating: A novel boundary engineering approach, J. Mater. Sci. Technol. 245 (2026)

249-255.

14. L.J. Huang, Q. An, L. Geng, S. Wang, S. Jiang, X.P. Cui, R. Zhang, F.B. Sun, Y. Jiao, X. Chen, C.Y. Wang, Multiscale architecture and superior high-temperature performance of discontinuously reinforced titanium matrix composites, Adv. Mater. 33(6) (2021) 2000688.
15. K.H. Jin, C. Liu, J.T. Ye, W.W. Yang, Y.C. Fang, X. Wei, J.Y. Jin, Q.Q. Ding, H.B. Bei, X.B. Zhao, Z. Zhang, Achieving enhanced tensile strength-ductility synergy through phase modulation in additively manufactured titanium alloys, Mater. Sci. Eng. A 909 (2024) 146801.
16. Y.J. Liang, H.M. Wang, Influence of prior-β-grain size on tensile strength of a laser-deposited α/β titanium alloy at room and elevated temperatures, Mater. Sci. Eng. A 622 (2015) 16-20.
17. Z.X. Zhang, S.J. Qu, A.H. Feng, J. Shen, Achieving grain refinement and enhanced mechanical properties in Ti-6Al-4V alloy produced by multidirectional isothermal forging, Mater. Sci. Eng. A 692 (2017) 127-138.
18. Z.F. Zhang, Z.G. Wang, Grain boundary effects on cyclic deformation and fatigue damage, Prog. Mater Sci. 53(7) (2008) 1025-1099.
19. H. Yang, M.X. Zhu, N.A. Chen, S.S. Xie, Y.H. Yu, G.D. Wang, C.Y. Wang, H.C. Kou, Novel hierarchical α structure enhanced strength-ductility synergy in metastable (3 titanium alloy, Mater. Sci. Eng. A 925 (2025) 147877.
20. X.F. Zhang, S. Wang, M.H. Hua, R.R. Chen, W.P. Xu, H.W. Wang, Oxygen-induced interfacial structure selection, dopant segregation and adhesive strength of α/β interfaces in titanium alloys, Scr. Mater. 267 (2025) 116813.
21. C.L. Zhang, X.Z. Li, S.Z. Li, J.Y. Zhang, G. Liu, J. Sun, Harnessing bifunctional nitrogen-dislocation interactions for a record ultra-strong-and-ductile duplex titanium alloy, Adv. Sci. 12(30) (2025) e02349.
22. J.G. Li, K.R. Zhang, R. Hu, J.R. Yang, Design and microstructure-mechanical properties of a novel metastable β titanium alloy with excellent strength-plasticity matching, J. Mater. Res. Technol. 28 (2024) 4177-4185.
23. R. Jain, R.S. Haridas, P. Awasthi, A. Dhal, R.S. Mishra, Evading strength-ductility trade-off in a metastability engineered layered metallic composite, Mater. Des. 252 (2025) 113786.
24. F. Sun, F. Prima, T. Gloriant, High-strength nanostructured Ti-12Mo alloy from ductile metastable beta state precursor, Mater. Sci. Eng. A 527(16-17) (2010) 4262-4269.
25. L.J. Meng, T. Kitashima, P. Lin, Z.H. Wang, Z.Y. Jiang, Q.X. Huang, J.W. Zhao, Achieving polymer-like ultrahigh elasticity in Ti-6Al-4V alloy via a new cryo-deformation induced α'-to-α" martensite phase transformation, Acta Mater. 293 (2025) 121109.
26. K.M. Li, X.C. Liu, Y.J. Liu, X. Wu, W.C. Zhang, J.J. Yang, W. Li, S.F. Zhou, Strengthening layer with nano-twins in titanium alloy induced by laser surface re-melting: Mechanism of high strength and ductility, Mater. Charact. 196 (2023) 112632.
27. S.Z. Wang, Z.H. Hu, Z.W. Huang, B. Gao, X.F. Chen, J.J. Hu, Y.T. Zhu, Y.S. Li, H. Zhou, New deformation mechanism and strength-ductility synergy in pure titanium with high density twin, Int. J.

Plast. 174 (2024) 103908.
28. J.C. Pang, S.X. Li, Z.G. Wang, Z.F. Zhang, General relation between tensile strength and fatigue strength of metallic materials, Mater. Sci. Eng. A 564 (2013) 331-341.
29. Y.Y. Zhao, M.T. Liang, S.J. Liu, W.H. Zhang, High-temperature fatigue behavior and cyclic deformation of a gradient nanostructured RAFM steel, Int. J. Fatigue 163 (2022) 107013.
30. X. Chen, L.J. Huang, S. Ma, F.B. Sun, S. Wang, L. Geng, Multi-scale dispersion strengthening for high-temperature titanium alloys: Strength preservation and softening mechanisms, J. Mater. Sci. Technol. 206 (2025) 1-14.
31. Z. Qu, Z.J. Zhang, R. Liu, L. Xu, Y.N. Zhang, X.T. Li, Z.K. Zhao, Q.Q. Duan, S.G. Wang, S.J. Li, Y.J. Ma, X.H. Shao, R. Yang, J. Eckert, R.O. Ritchie, Z.F. Zhang, High fatigue resistance in a titanium alloy via near-void-free 3D printing, Nature 626(8001) (2024) 999-1004.
32. J.W. Liu, K. Zhang, M.J. Bermingham, H.L. Fraser, P. Hodgson, M. Heilmaier, A. Boretti, Y.M. Zhu, A.J. Huang, Fatigue and damage tolerance performance of additively-manufactured titanium alloys for structural application: A comprehensive review, Mater. Sci. Eng. R Rep. 167 (2026) 101135.
33. Y. Chong, T. Bhattacharjee, J.H. Yi, A. Shibata, N. Tsuji, Mechanical properties of fully martensite microstructure in Ti-6Al-4V alloy transformed from refined beta grains obtained by rapid heat treatment (RHT), Scr. Mater. 138 (2017) 66-70.
34. Z.Y. Zou, M. Simonelli, J. Katrib, G. Dimitrakis, R. Hague, Microstructure and tensile properties of additive manufactured Ti-6Al-4V with refined prior-? grain structure obtained by rapid heat treatment, Mater. Sci. Eng. A 814 (2021) 141271.
35. Q.S. Pan, L. Lu, Improved fatigue resistance of gradient nanograined metallic materials: Suppress strain localization and damage accumulation, Scr. Mater. 187 (2020) 301-306.
36. H.L. Chen, X.M. Luo, M.Y. Zhang, M. Wen, X.F. Zhu, G.P. Zhang, More severe surface relief but stronger fatigue resistance at small scales: Vacancy-assisted fatigue damage mechanism, Acta Mater. 274 (2024) 120028.
37. Z. Niu, Y. Lei, Y.Y. Liu, B. Gao, Y. Sun, Z. Wang, Rotary bending fatigue behavior of maraging steel with an anisotropic gradient nanostructured surface layer, J. Mater. Sci. Technol. 259 (2026) 15-25.
38. G. Wang, Y. Zhang, J. Liu, W. Chen, K. Wang, B. Cui, B.K. Zou, Q.B. Ouyang, Y.M. Zhang, Z.Y. Hu, L. Wang, W.T. Yan, S.B. Jin, J. Ding, Y.M. Wang, T. Zhu, Z. Li, D. Zhang, E. Ma, Dispersion hardening using amorphous nanoparticles deployed via additive manufacturing, Nat. Commun. 16(1) (2025) 3589.
39. Y.M. Zhu, K. Zhang, Z.C. Meng, K. Zhang, P. Hodgson, N. Birbilis, M. Weyland, H.L. Fraser, S.C.V. Lim, H.Z. Peng, R. Yang, H. Wang, A.J. Huang, Ultrastrong nanotwinned titanium alloys through additive manufacturing, Nat. Mater. 21(11) (2022) 1258-1262.
40. Y.M. Mao, Q.Y. Zhao, R.Q. Zhang, P. Guo, Y.N. Chen, Y.Q. Zhao, Trifunctional local-range order oxygen structure enhanced strength-ductility and fatigue resistance in large-scale metastable titanium alloy, Nat. Commun. 16(1) (2025) 7168.

41. C.L. Zhang, J.Y. Zhang, X.Y. Bao, J. Li, D.D. Zhang, G. Liu, J. Sun, Hierarchically ordered coherent interfaces-driven ultrahigh specific-strength and toughness in a nano-martensite titanium alloy, Acta Mater. 263 (2024) 119540.
42. Z. Zhao, J. Chen, S. Guo, H. Tan, X. Lin, W.D. Huang, Influence of α/β interface phase on the tensile properties of laser cladding deposited Ti-6Al-4V titanium alloy, J. Mater. Sci. Technol. 33(7) (2017) 675-681.
43. X.F. Ding, S.Z. Yuan, B.Q. Jin, X.F. Zhang, L. Yang, L.Z. Zhao, Y.Q. Chen, M.B. Wang, Y. Liu, Y.F. Song, Improving the high-temperature tensile properties of titanium alloys by elemental enrichment at grain boundaries, Mater. Charact. 229 (2025) 115609.
44. H.H. Li, E.J. Sun, K. Wang, Influence of lamellar-α geometry characteristics on mechanical properties of bimodal microstructure in Ti-6Al-4V alloy, Mater. Sci. Eng. A 927 (2025) 148018.
45. Q.H. Jiang, B.B. He, S. Li, C.L. Yang, W. Fan, M. Fu, B. Zhang, Hierarchically ultrafine grains with the embedded nanotwins structure produced in ultra-high strain rate deformation of coarse-grained titanium alloy, J. Mater. Process. Technol. 345 (2025) 119070.
46. W.W. Yang, X. Wei, K.H. Jin, J.T. Ye, Z.J. He, Q.Y. Lin, Z.M. Wu, X.C. Sun, C. Liu, Q.Q. Ding, H.B. Bei, X.B. Zhao, Z. Zhang, In-situ α-phase and TiB modulation for enhanced strength-ductility synergy in laser-directed energy deposited Ti-Al-V-Fe-B Alloy, Addit. Manuf. 109 (2025) 104839.
47. Z.M. Liu, S.W. Xin, Y.Q. Zhao, Decoupling the elemental contributions of Al, Zr and Mo to the thermal stability of high-temperature titanium alloys, J. Mater. Res. Technol. 39 (2025) 8852-8864.
48. S.Z. Zhang, H.Q. Zhang, C.J. Zhang, X.Y. Zhang, R.P. Liu, Achieving outstanding room and high-temperature mechanical properties matching in a near α high-temperature titanium alloy with fine lamellar microstructure and nanosilicides, J. Mater. Sci. Technol. 229 (2025) 30-35.

Figures

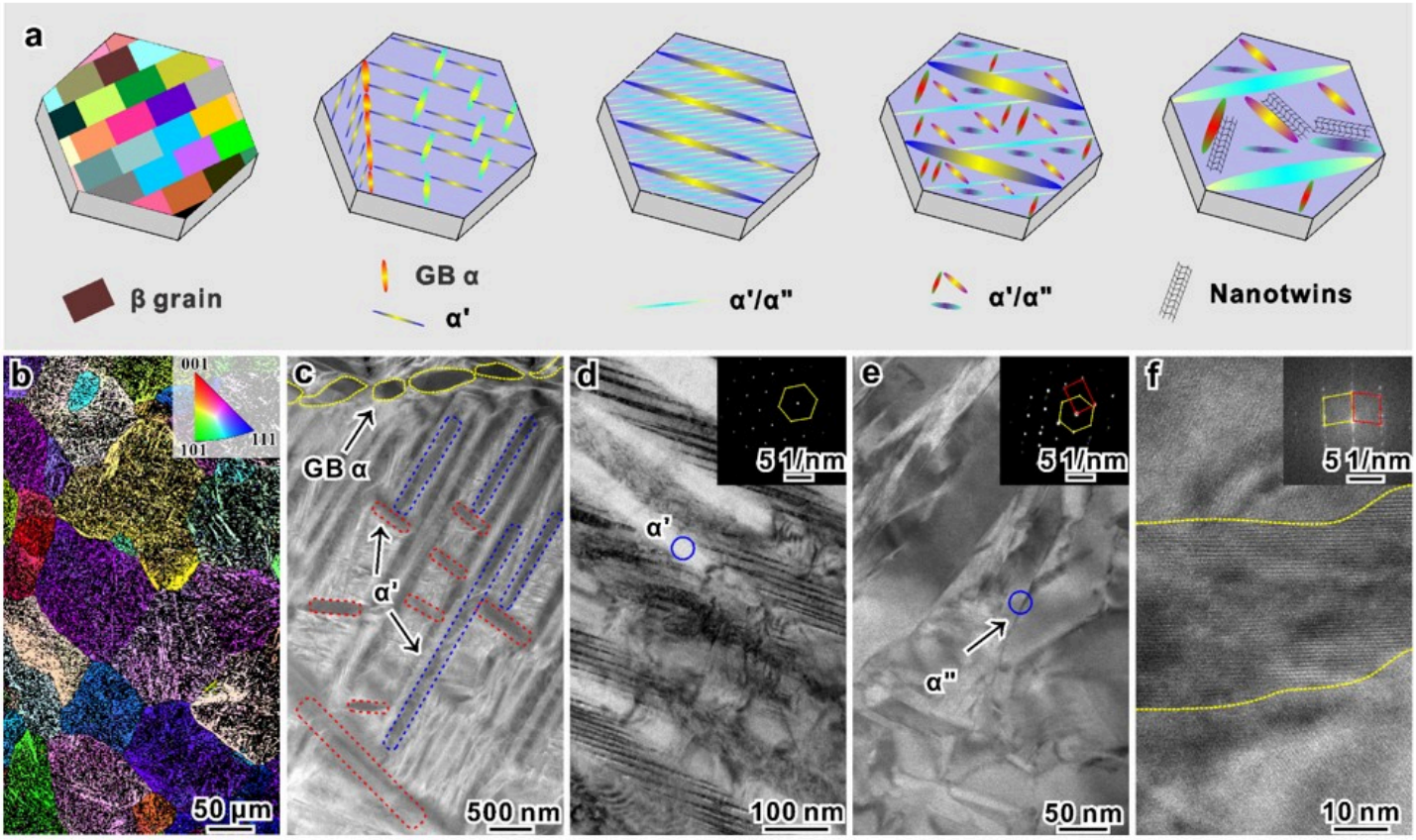


Figure 1

MHIN microstructure design strategy of the Ti-6.5Al-3.5Mo-1.5Zr-0.3Si alloy by RTP. a Schematic of the integrated strengthening mechanisms across different length scales. **b** AM yields confined β-phase columnar grains at the micrometer scale. **c** A fragmented α colony structure forms as the growth of α sheets with identical orientations is mutually inhibited at the sub-micron scale. **d** Nanoscale interwoven α' further enhances interfacial strength. **e** Lattice distortion resulting in ultrafine α" precipitates. **f** Coherent nanotwins provide additional barriers to dislocation motion.

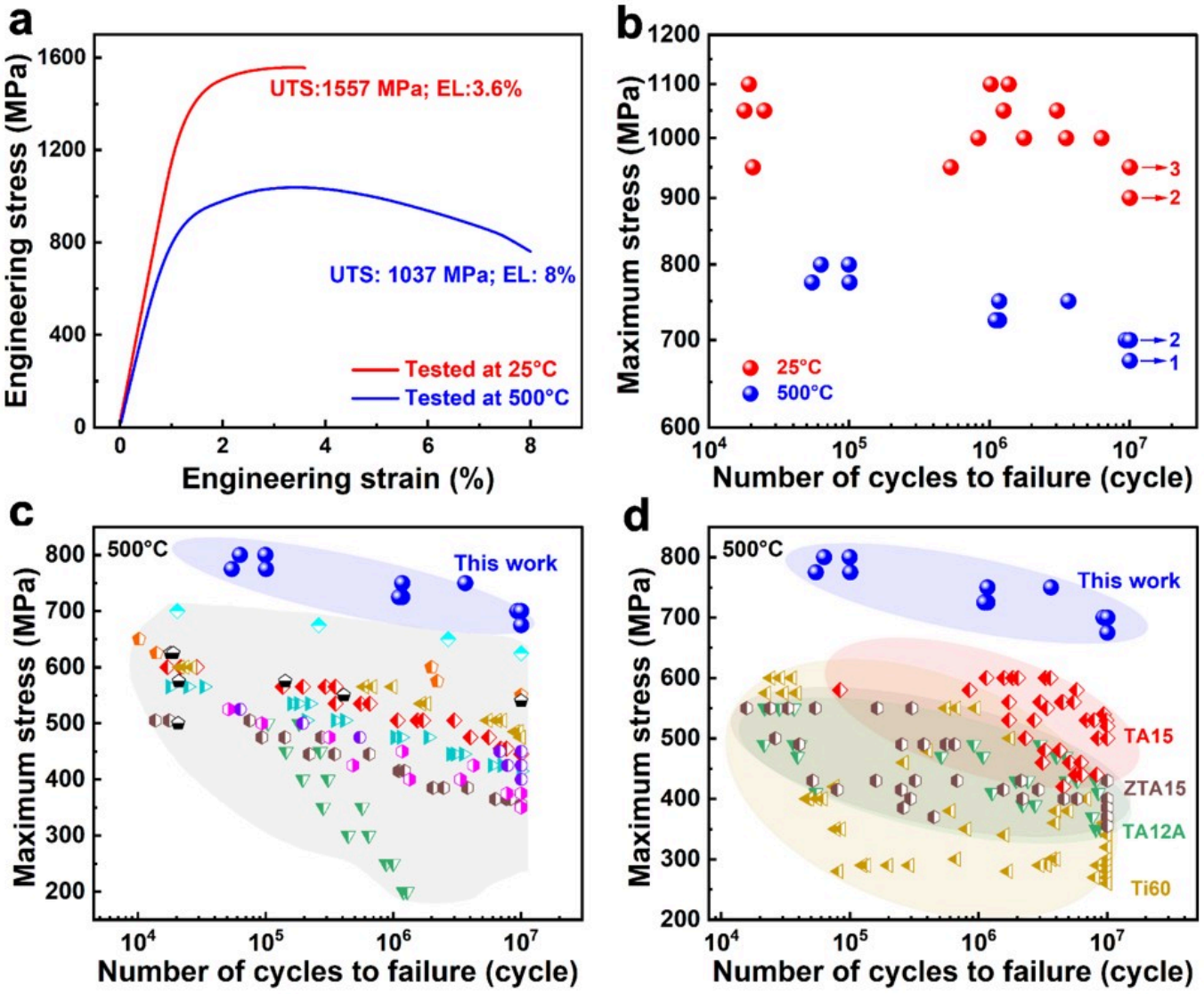


Figure 2

Tensile and HCF performances of the MHIN alloy. a Engineering stress-strain curves at ambient temperature and 500 °C. **b** Stress-life (*S-N*) curves at a stress ratio $R = 0.1$ for ambient temperature and 500 °C. **c** Fatigue life of the current alloy compared with reported data for Ti-6.5Al-3.5Mo-1.5Zr-0.3Si at 500 °C. **d** Fatigue life of the present alloy versus reported values for other titanium alloys at 500 °C (sources detailed in Tables S2 and S3).

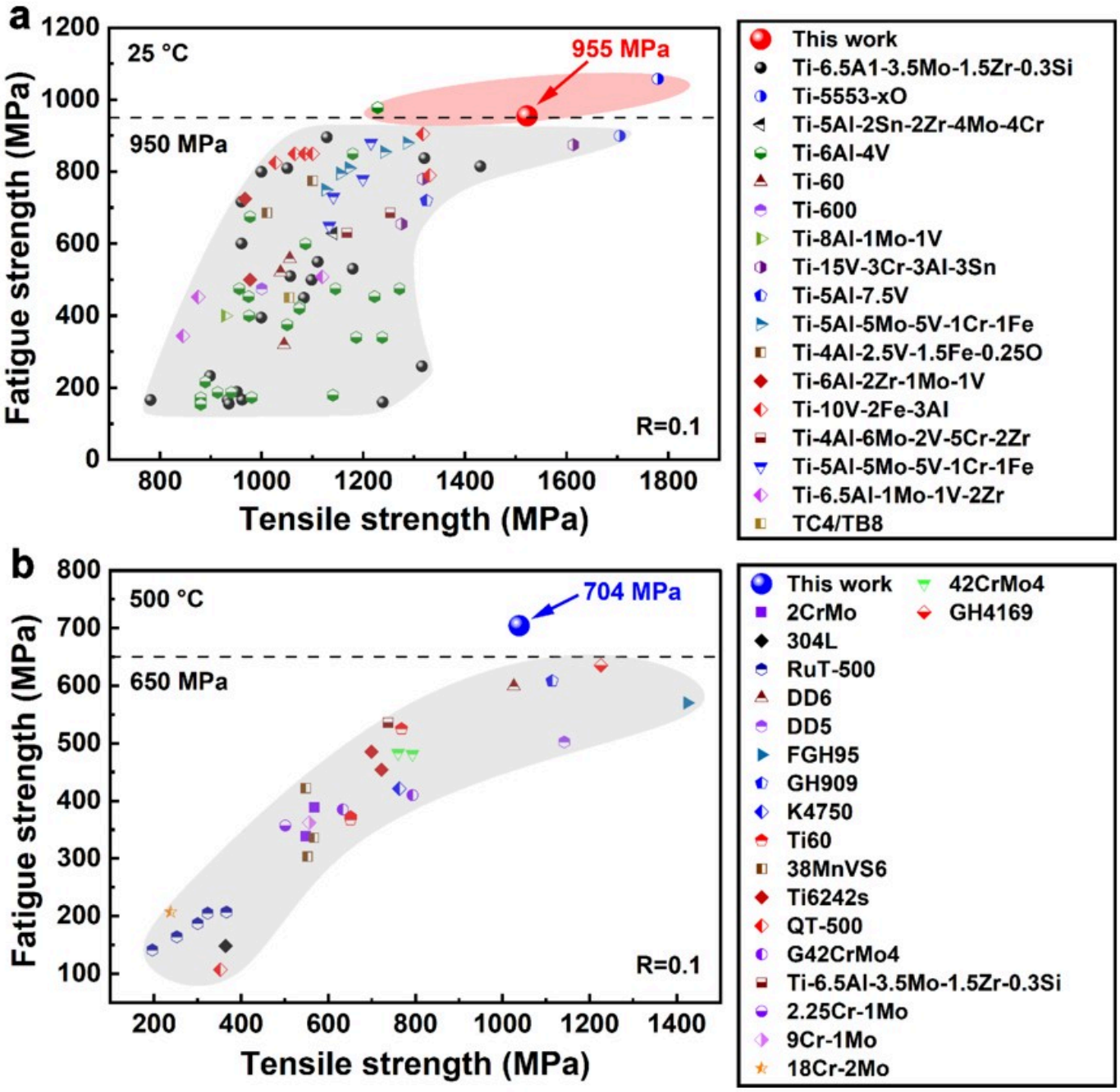


Figure 3

Evaluation of fatigue strength versus tensile strength at ambient temperature and 500 °C. a The tensile-fatigue strength comparison of the present alloy with other reported titanium alloys at ambient temperature (data sources are listed in Table S4). **b** Fatigue strength-tensile strength correlation for the current alloy and various high-temperature alloys from literature at 500 °C (data sources are listed in Table S5).

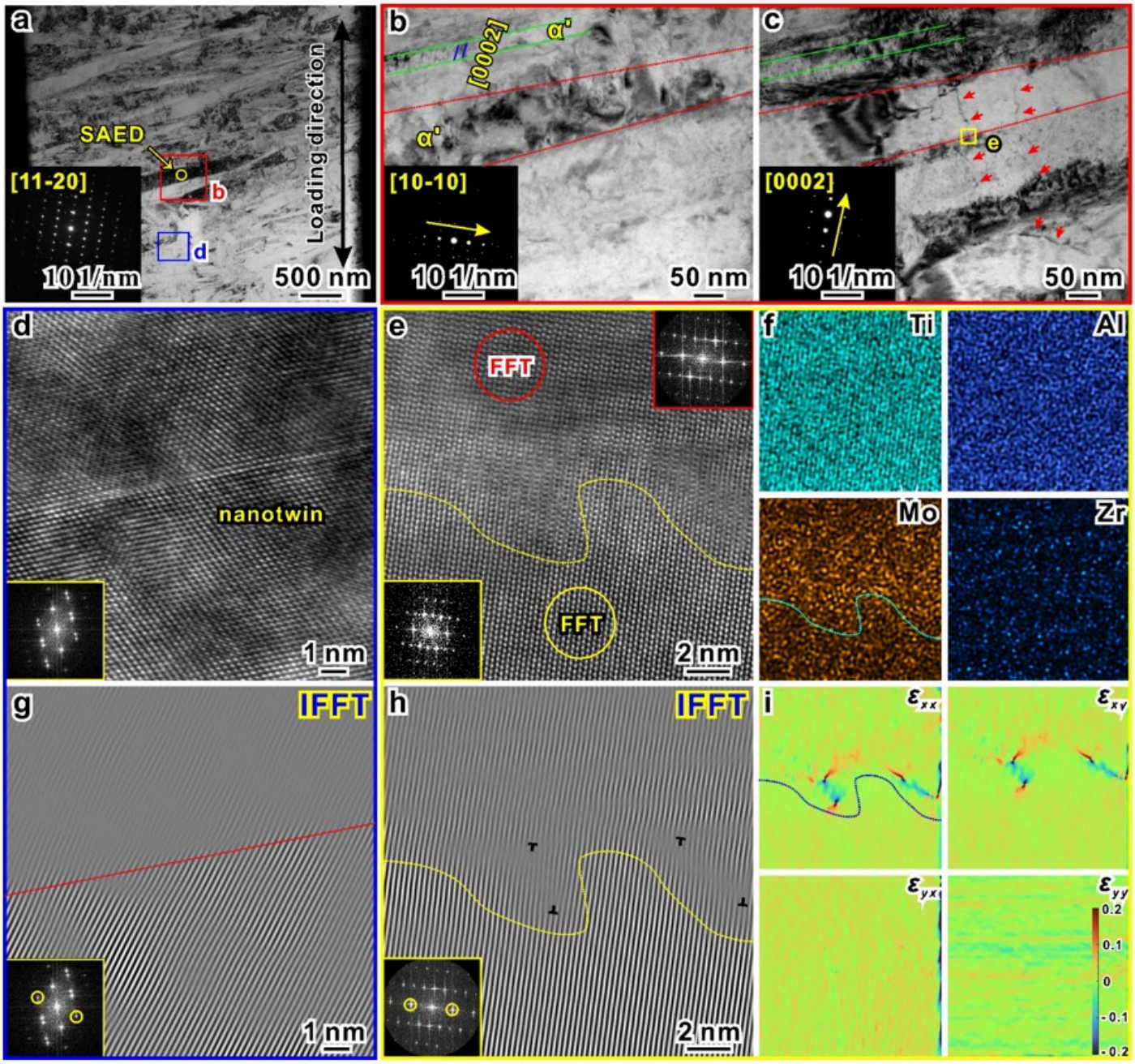


Figure 4

Micro-deformation substructures of fatigue damage in MHIN alloy tested at ambient temperature (σ_{max} = 1000 MPa, N_f = 3.51×10^6 cycles): **a** Sub-surface microstructure of the crack initiation area. **b, c** Dislocation analysis performed within region b using the $g \cdot b$ = 0 criterion under two-beam diffraction conditions in SAED patterns. **d, g** HRTEM image of nanotwins observed in region d of **a**, along with the corresponding IFFT analysis results. **e** HRTEM image of the boundary features of region e in image **c**. **f, h, i** the corresponding STEM-EDS, IFFT, and GPA analyses conducted on the region shown in **e**.

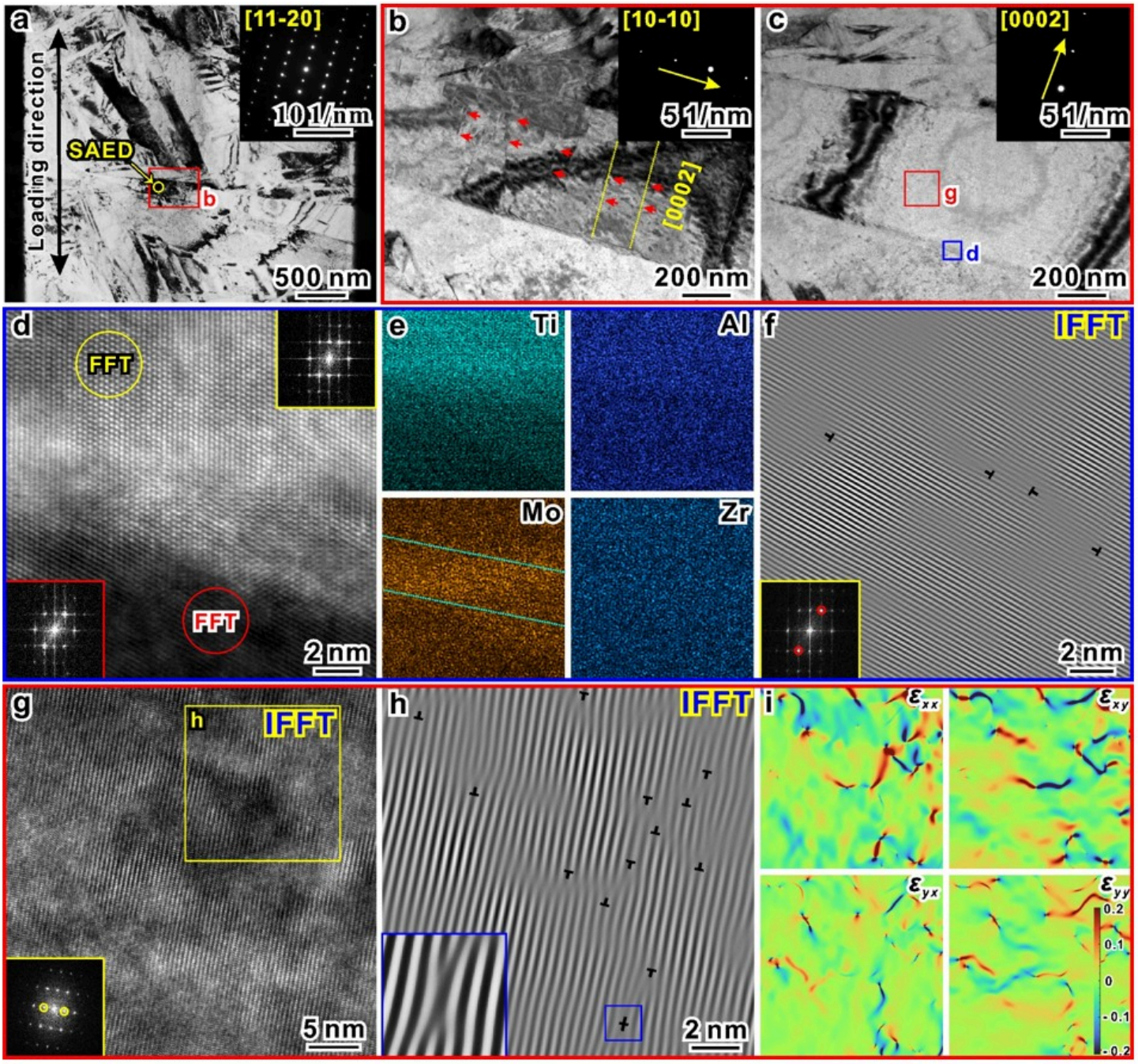


Figure 5

Micro-deformation substructures of fatigue damage in MHIN alloy tested at 500 ℃ (σ_{max} = 700 MPa, N_f = 9.34×10^6 cycles): a Sub-surface microstructure of the crack initiation area. **b**, **c** Dislocation analysis conducted within region b via the $g \cdot b$ = 0 criterion under two-beam diffraction conditions using SAED patterns. **d** HRTEM image of the boundary features of region d in image **c**. **e** STEM-EDS analysis performed on **d**. **f** IFFT analysis derived from in image **d**. **g** HRTEM image of region g indicated in **c**. **h, i** IFFT and GPA analysis derived from region h in **g**.

Supplementary Files

This is a list of supplementary files associated with this preprint. Click to download.

- Supplementarymaterials.docx